Bionic grinding machine design for thin shell removal from cassia seeds

Xinyu Yuan[1], Caojun Huang[2*], Xuewen Gao[3], Shangyu Tong[4], Yifei Li[1], Shujuan Yi[1]

(1. *College of Engineering, Heilongjiang Bayi Agricultural University, Daqing 163711, Heilongjiang, China*;
2. *College of Information and Electrical Engineering, Heilongjiang Bayi Agricultural University, Daqing 163711, Heilongjiang, China*;
3. *Weichai Lovol Heavy Industry Co., Ltd., Weifang 261200, China*;
4. *College of Environmental Ecology, Tibet University, Lhasa 850013, China*)

Abstract: In order to address the challenge of low efficiency in removing the thin shells from cassia seeds, a bionic grinding machine was developed for the removal of thin shells from cassia seeds during pharmaceutical processing, inspired by the hand-rubbing motion observed in traditional manual methods. The machine features a grinding-suction disk assembly integrated with a negative-pressure feeding system. Flow rate calculations were performed to support the design, although specific parameters require further elaboration. A single-chip microcontroller (SCM)-based control system enables real-time parameter adjustment via a human–machine interface, ensuring precise control throughout the grinding process. After prototype fabrication, single-factor experiments established parameter ranges for orthogonal testing. The optimal parameter combination was identified as a grinding layer gap of 2.4 mm, a rotational frequency of 170 r/min, and a grinding duration of 12 s, resulting in a grinding degree of 9.07% and a shell removal cleanliness of 4.51%. Image-based surface feature analysis confirmed the machine's effectiveness in removing thin shells, supporting its applicability in pharmaceutical seed processing. This study introduces a novel and efficient mechanized approach for cassia seed thin shell removal, which enhances the efficiency of thin shell removal and provides meaningful support for the advancement of pharmaceutical seed processing technologies.

Keywords: cassia seed, grinding, automatic control system, test, light reflectivity
DOI: 10.25165/j.ijabe.20251806.9532

Citation: Yuan X Y, Huang C J, Gao X W, Tong S Y, Li Y F, Yi S J. Bionic grinding machine design for thin shell removal from cassia seeds. Int J Agric & Biol Eng, 2025; 18(6): 269–280.

1 Introduction

As quality of life improves, there has been a growing emphasis on healthcare, resulting in increased global demand for Chinese herbal medicine. Recent data indicate that these traditional remedies are gradually being integrated into international medical systems[1,2]. Among them, cassia seeds have been a fundamental component of traditional Chinese medicine for thousands of years[3]. In recent clinical applications, ointments formulated from cassia seeds have demonstrated high efficacy in treating dermatological conditions such as tinea corporis[4], and have reportedly been used in tens of thousands of cases[5]. However, in accordance with pharmaceutical preparation standards, the presence of a thin shell on the seed surface can affect the quality of the final medicinal product. Therefore, non-destructive grinding is essential to effectively remove these thin shells prior to processing. At present, this de-shelling process is performed manually, relying on traditional grinding techniques. However, as market demand grows, the drawbacks of manual processing—such as low efficiency, poor precision, and high labor costs—have become increasingly prominent.

Research on grinding machines specifically designed for cassia seeds and other Chinese medicinal herbs remains limited. In related domains, the working principles of hulling machines for agricultural crops and polishing machines used in industrial surface treatment are generally classified into three categories: extrusion[6,7], kneading[8-10], and impact[11,12]. The production of hulled grains—such as rice, wheat, and sorghum—often involves the removal of seed coats through the controlled flow of raw materials within the system[13-15]. These systems typically utilize a combination of rubber rollers and screens to form an axial flow channel, drawing inspiration from traditional stone mills. Friction between the seeds and the screen facilitates the removal of seed coats, with the mesh size and the gap between the rollers and screen determining the grinding effectiveness.

In industrial applications, surface polishing processes—such as removing lacquer or enhancing the appearance of workpieces—often rely on materials with varying levels of abrasiveness (e.g., wool, sponge, rabbit fur)[16,17]. For harder materials like gemstones or metals, more intensive material removal is required to meet surface quality standards. These processes frequently employ waterjet polishing or metal tools combined with coolants to achieve the desired finish[18–21]. However, due to the unique morphology and mechanical properties of cassia seeds—as well as the stringent quality standards required for medicinal use—these conventional grinding and polishing techniques are unsuitable for achieving precise and non-destructive removal of their thin shells.

This study addresses the specific requirements of pharmaceutical processing for cassia seeds by designing a grinding machine tailored for thin shell removal. The structural parameters of

Received date: 2024-11-13 **Accepted date:** 2025-08-01
Biographies: Xinyu Yuan, PhD, research interest: design and manufacturing of agricultural equipment, Email:yuanxinyu97@163.com; **Xuewen Gao**, MS, research interest: design and manufacturing of agricultural equipment automation, Email: 617128399@qq.com; **Shangyu Tong**, PhD candidate research interest: design and manufacturing of agricultural equipment automation, Email: tongshangy@163.com; **Yifei Li**, PhD candidate research interest: design and manufacturing of agricultural equipment, Email: liyifei1990@126.com; **Shujuan Yi**, PhD,Professor, research interest: design and manufacturing of agricultural equipment, Email: yishujuan2005@126.com.
***Corresponding author: Caojun Huang**, PhD, Professor, research interest: design and manufacturing of agricultural equipment automation, College of Information and Electrical Engineering, Heilongjiang Bayi Agricultural University, Daqing 163711, China. Tel: +86-13836961966, Email: huangcaojun@126.com.

the primary functional components were determined based on the mechanical properties and morphology of the seeds. An automated control system with a human–machine interface was developed, enabling real-time adjustment of key parameters such as grinding time, rotational speed, and applied pressure. Finally, performance testing was conducted to evaluate the machine's effectiveness, confirming its capability to achieve efficient and non-destructive thin shell removal in accordance with pharmaceutical quality standards.

2 Materials and methods

2.1 Physical properties of cassia seeds

2.1.1 Triaxial dimensions

Figure 1a illustrates the shape of cassia seeds, which are brown, column-like structures with sharp, parallel ends. To clearly represent their characteristic dimensions, a Cartesian coordinate system was introduced (Figure 1b). A total of 300 cassia seeds were randomly selected and divided into three groups for measuring their triaxial dimensions. The resulting data were organized into a tabular format, as presented in Table 1.

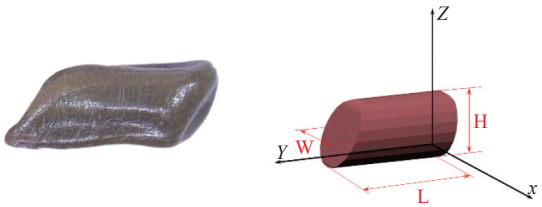

a. Shape b. Size

Figure 1 Diagram of cassia seed

Table 1 Triaxial dimensions of cassia

Project	Minimum	Maximum	Mean
Length/mm	2.64	6.07	4.77
Width/mm	1.38	2.96	2.08
Height/mm	1.24	3.63	2.10

2.1.2 Mechanical property

Regulating the distance between the upper and lower grinding disks is essential for controlling the grinding and polishing effects applied to cassia seeds. To determine the maximum compressive pressure that the seeds can withstand, a universal testing machine was employed to measure the ultimate pressure under three different compression orientations. The testing apparatus and corresponding compression directions are illustrated in Figure 2. Representative compression images for each orientation are shown in Figure 3, and the measured ultimate pressures are summarized in Table 2.

Notable differences in ultimate pressure were observed among the three orientations. In the lateral and lie orientations, the seed dimensions along the direction of force application—defined as height and width, respectively—are smaller, resulting in relatively consistent pressure resistance. However, in the lie orientation, greater displacement under polar pressure was recorded, suggesting a direct relationship between deformation and polar pressure. In contrast, in the standing orientation, the sharper ends of the seed facilitate the concentration of external forces, leading to an earlier failure point and reduced load-bearing capacity.

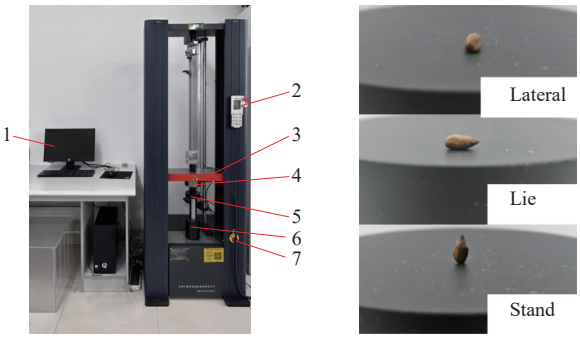

a. Testing machine b. Compression orientation

Note: 1. Calculator; 2. Remote controls; 3. Moving beam; 4. Upper plate; 5. Lower plate; 6. Underlay; 7. Emergency stop switches.

Figure 2 Schematic diagram of extreme pressure test

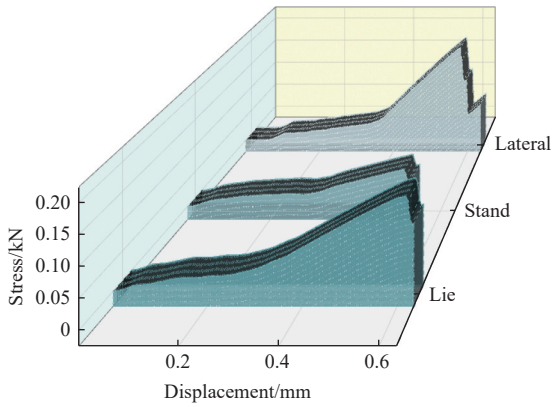

Figure 3 Pressure/displacement images of cassia

Table 2 Compression orientations of cassia

Project	Minimum	Maximum	Mean
Lateral/kN	0.084	0.157	0.114
Lie/kN	0.088	0.155	0.123
Stand/kN	0.054	0.066	0.052

2.1.3 Friction property

According to the principles of grinding, analyzing the grinding action requires calculating the friction between cassia seeds and the silicone grinding plate. To determine the static friction coefficient and rolling friction coefficient, a custom-built inclinometer was used. The testing procedure is illustrated in Figure 4.

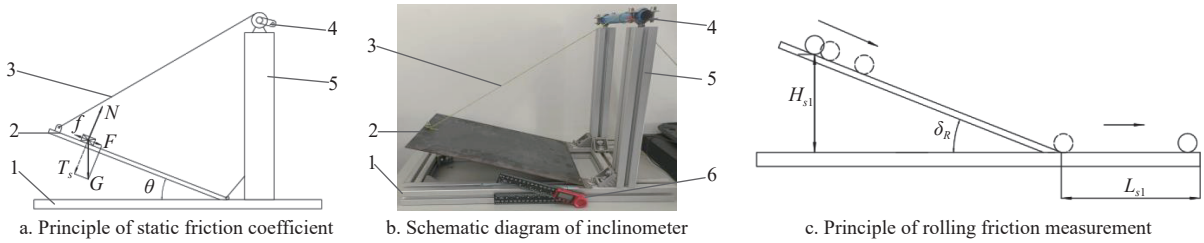

a. Principle of static friction coefficient measurement b. Schematic diagram of inclinometer c. Principle of rolling friction measurement

Note: 1. Base 2. Inclined plate 3. Towing rope 4. Spool 5. Straight arm 6. Angle ruler.

Figure 4 Static friction coefficient test procedure

By gradually raising the height of the prototype material plate to increase the inclination angle of the inclined surface, the point at which the cassia seeds begin to slide was observed. The inclination angle at the onset of sliding, denoted as θ, was recorded. This angle was then substituted into Equation (1) to calculate the static coefficient of friction between the cassia seeds and the surface of the prototype material.

$$\mu_s = \frac{G\sin\theta}{G\cos\theta} = \tan\theta \tag{1}$$

where, μ_s is the static friction coefficient; G is the gravitational force of the Cassia seeds, N; θ is the angle of inclination of the inclined plane, (°).

Cassia seeds were placed on an inclined plane set at an inclination angle δ_R of 30°, with a height Hs_1=0.1 m. Prior to measurement, a partition plate was used to hold the seeds in place, ensuring that their initial velocity was 0. Upon removal of the partition, the seeds were allowed to fall freely under static conditions. The horizontal rolling distance after landing, denoted as L_{s1}, was recorded. This value was then substituted into Equation (2) to calculate the rolling friction coefficient between the cassia seeds and the silicone plate.

$$\mu_r = \frac{H_{s1}}{L_s + \dfrac{H_{s1}}{\tan\delta_R}} \tag{2}$$

where, μ_r is the rolling friction coefficient; H_{s1} is the height of the inclined plane, mm; L_{s1} is the rolling distance, mm; and δ_R is the angle of inclination of the inclined plane.

With reference to the above method, the static friction coefficient and rolling friction coefficient between cassia seeds and silica gel plate were measured respectively, five seeds were randomly selected for measurement, and each seed was measured three times, and the measurement results were organized as shown in Table 3. The coefficient of static friction between cassia seeds and silica gel was 0.6-0.7, and the coefficient of rolling friction was 0.05-0.06.

Table 3 Friction coefficient test results

No.	1		2		3		4		5	
	Static	Rolling	Static	Rolling	Static	Rolling	Static	Rolling	Static	Rolling
1	0.62	0.051	0.61	0.053	0.68	0.058	0.73	0.057	0.66	0.056
2	0.58	0.052	0.62	0.054	0.67	0.059	0.72	0.056	0.65	0.057
3	0.59	0.047	0.63	0.052	0.71	0.063	0.72	0.055	0.60	0.055
Ave	0.60	0.050	0.62	0.053	0.70	0.060	0.70	0.056	0.63	0.055

2.2 Structure working principle of grinding machine

The overall structure of the cassia seed grinding machine is shown in Figure 5, with its technical specifications listed in Table 4. The main components of the machine include the panning structure, grinding and polishing mechanism, negative pressure system, lifting system, scraping mechanism, feeding mechanism, and transportation mechanism.

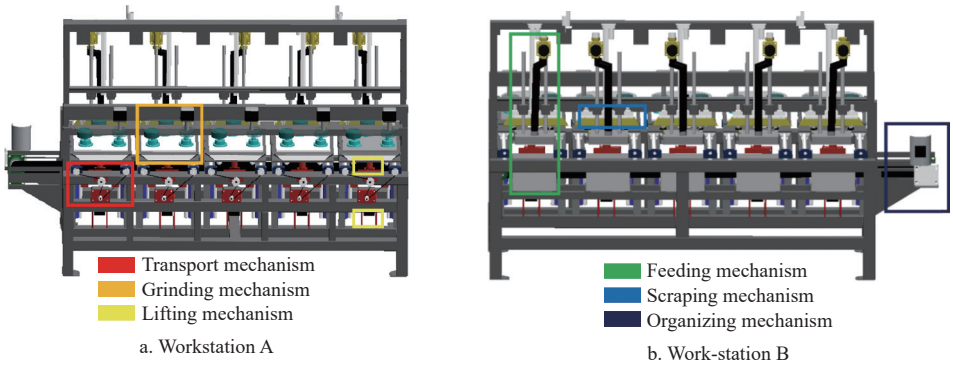

Figure 5 Schematic diagram of grinding machine

Table 4 Technical parameters of grinding machine

Project	Parameter
Size (length, width, and height)/mm	3100×1200×1700
Mass/kg	1000
Nominal voltage/V	380
Power supply type	Alternating current
Rating/W	3000
Work efficiency/kg·h^{-1}	100
Number of rows	5

During operation, the negative pressure system provides suction to the feeding mechanism. The suction box extracts cassia seed raw material from the feed container and deposits it onto the lower grinding disk at Workstation A. The transport mechanism then moves the lower grinding disk from Workstation A to Workstation B. Once in position, the lifting system elevates the lower disk to a predetermined height. At this point, the upper grinding disk, driven by the grinding motor, begins to rotate to initiate the grinding process.

After grinding is complete, the lifting system resets, allowing the lower grinding disk to descend. Simultaneously, the upper grinding disk performs a secondary rotation to complete the final stage of the grinding cycle. As the lower disk descends, the transport mechanism shifts it from Workstation B back to Workstation A. During this transition, the scraping plate moves downward to remove the processed product from the disk surface and transfers it onto the conveyor belt of the transport mechanism for centralized collection and storage.

2.3 Design of key components

2.3.1 Grinding mechanism

Cassia seeds naturally rest in an upright orientation, standing vertically along their short axis (the seed's narrower dimension) when placed on a flat surface. To ensure uniform grinding of the seed surface, the seeds must be induced to rotate in coordination with the upper grinding disk. Figure 6 illustrates the working principle of the cassia seed grinding machine.

The grinding mechanism comprises an upper fixed disk, bearing seat, lower fixed disk, auxiliary inoculation plate, lower grinding disk, upper grinding disk, and an eccentric bearing, as schematically illustrated in Figure 7.

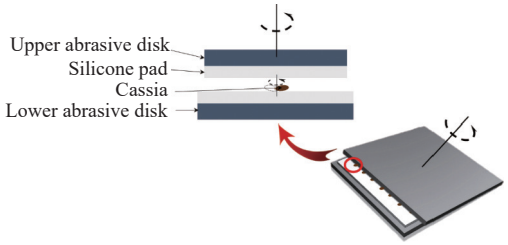

Figure 6 Schematic diagram of the cassia seed grinding

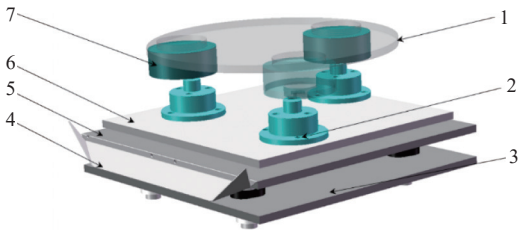

Note: 1. Upper fixed disk 2. Bearing seat 3. Lower fixed disk 4. Auxiliary inoculation plate 5. Lower grinding disk 6. Upper grinding disk 7. Eccentric bearing

Figure 7 Schematic diagram of the grinding mechanism

As shown in Figure 6, during the grinding process, cassia seeds are placed on the lower grinding disk. With the rotation of the upper grinding disk, the seeds undergo synchronous rotation between the upper and lower disks while simultaneously rotating along their own longitudinal axis. Taking gravity as the vertical reference direction, the forces acting on the cassia seed are projected onto the vertical rotational plane. The resulting force analysis diagram for this motion process is illustrated in Figure 8. The seeds are primarily subjected to their own weight G, the normal support force F_{N1} from the lower grinding disk, the applied pressure F_{N2} from the upper grinding disk, the static friction force f_1 from the upper grinding disk, the rolling friction force f_2 between the seed and the lower grinding disk, and the centrifugal force F_E generated by the rotation.

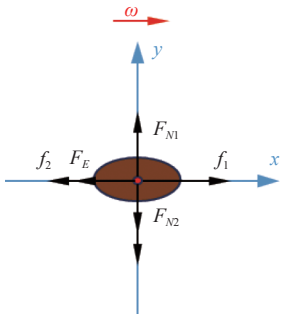

Figure 8 Schematic diagram of forces acting on cassia seed during the grinding process

The forces in both the y-direction and x-direction are analyzed, and their relationship is expressed in Equation (3).

$$\begin{cases} F_{N1} = F_{N2} + G \\ f_1 = f_2 + F_E \\ F_E = m\omega R^2 \\ f_1 = \mu_s G \\ f_2 = \mu_r F_{N2} \end{cases} \quad (3)$$

where, m denotes the mass of a single cassia seed, g; ω is the angular velocity of both the upper grinding disk and the seed, rad/s; and R represents the rotational radius of the cassia seed, mm.

1) Lower grinding disk

Based on the triaxial dimensions of cassia seeds, the size of the lower grinding disk was determined. The disk's dimensions are directly related to both the number of seeds processed per cycle and the characteristic size of the cassia seeds. The dimensional parameters of the lower grinding disk are illustrated in Figure 9 and conform to the following equation:

$$X_1 = n \cdot L_{max} + (n+1)\, r \quad (4)$$

In the equation, X_1 is the circumference of the lower grinding disk, mm; r is the distance between the edge grinding position and the edge of the lower grinding disk, mm; L_{max} is the maximum triaxial dimension of the cassia seed, mm; n is the number of cassia seeds ground in a single row.

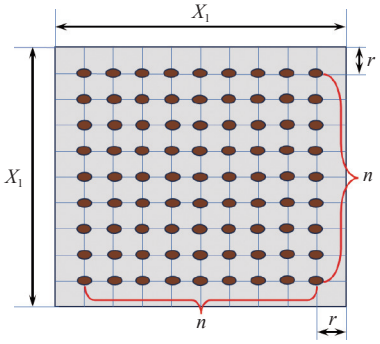

Figure 9 Schematic diagram of the lower grinding disk

Based on the analysis of the cassia seed grinding process, the spacing r between two adjacent cassia seeds is influenced by their rotational radius R. However, due to the irregular shape of the seeds, there is inherent uncertainty in the value of R. Possible variations in rotational radius caused by different seed orientations are illustrated in Figure 10.

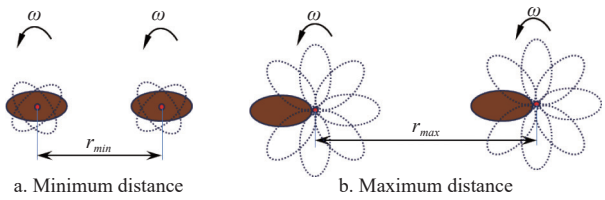

Figure 10 Schematic diagram of cassia spinning program

To accommodate potential eccentric rotation, the maximum offset—based on the seed's triaxial dimensions—must be considered. To prevent rotational interference, the distance between neighboring seeds should satisfy the following equation:

$$r \geq 5L_{max} \quad (5)$$

To balance grinding effectiveness with the operational efficiency of the machine, the minimum feasible value of r is selected, incorporating the maximum triaxial dimensions of the cassia seeds into the calculation. Based on this, the dimensions of the grinding disk are determined as follows:

$$X_1 = (3n+1) \cdot L_{max} \quad (6)$$

In accordance with the specifications of the production process, the value of n is fixed at 10 and subsequently used to calculate the dimensions of the lower grinding disk, which are determined to be 300 mm in diameter.

2) Upper grinding disk

The upper grinding disk serves as the active component

responsible for the grinding motion. Its size must be sufficient to fully cover all cassia seeds on the lower disk, while avoiding excessive dimensions that would unnecessarily increase the overall footprint of the machine. Therefore, the size of the upper grinding disk should be determined with reference to that of the lower grinding disk.

$$X_2 = n \cdot L_{\max} + nr \tag{7}$$

Therefore, the diameter of the upper grinding disk is set to 240 mm, allowing for a grinding displacement of 30 mm during operation.

3) Grinding layer gap

According to the principles of grinding and polishing, both the upper and lower grinding plates are covered with silicone pads of identical dimensions, forming the grinding layer. A food-grade silicone pad with dimensions of 300×300 mm, a thickness of 5 mm, Shore A hardness of 10°, and a Young's modulus of 0.5 MPa is selected as the grinding layer material. The calculation method for its elastic deformation coefficient is as follows:

$$k = \frac{EA}{h} \tag{8}$$

where, E represents the elastic modulus, N/m^2; A is the contact area under load, m^2; h is the thickness, m.

With the elastic recovery coefficient of the silicone pad determined as k=20 N/mm, the calculation method for the effective pressure exerted on cassia seeds is as follows:

$$F_{N2} = k \cdot (L_{\max} - p) \tag{9}$$

where, F is the pressure exerted by the grinding layer on the cassia seeds, N; k is the elastic recovery coefficient of the silicone pad, N/mm; p is the grinding layer gap, mm.

Based on the measured mechanical properties of cassia seeds, to achieve a non-destructive grinding effect, the effective pressure F_{N2} must be less than the minimum value of the seed's compressive strength in all directions, i.e., F_{N2}<52 N. Substituting into the equation yields a required pressure p<3.6 mm.

According to the triaxial dimension results of the cassia seeds, the grinding layer gap must also be greater than the minimum value of the seeds' triaxial dimensions.

As a result, the calculated range for the grinding layer gap was determined to be 1.2-3.6 mm, with the optimal value later verified through experimental testing.

4) Eccentric bearing

The grinding of cassia seeds is achieved through a bionic human motion, specifically a rubbing action akin to the movement of both palms. If the upper grinding disk were directly connected to the drive motor, centrifugal force would cause the cassia seeds to splash. To address this, the motor is connected via eccentric bearings and a bearing housing, enabling reciprocating rotational motion of the upper grinding disk. To ensure stability, a three-point mounting is used to drive the upper grinding disk, as shown in Figure 11. For ease of installation and subsequent maintenance, the eccentric bearing located in the lower right corner is linked to the drive motor, with the other two bearings acting as passive components. The amplitude of the grinding motion is equal to half the difference in size between the upper and lower grinding disks. Therefore, an eccentric bearing with a 30 mm eccentric distance is selected.

2.3.2 Feeding mechanism

The loading structure of the grinding and polishing machine is designed to enable single-grain adsorption of raw materials within the material box via negative pressure. The main components include electric push rods, suction boxes, material boxes, and restrictors. A schematic of the configuration is shown in Figure 12.

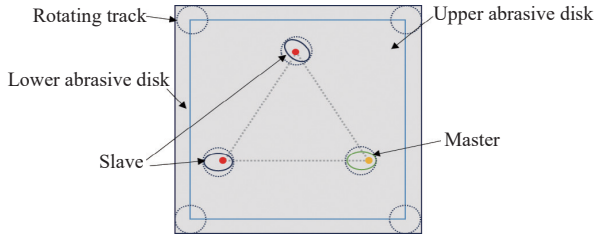

Figure 11 Schematic diagram of the upper grinding disk drive

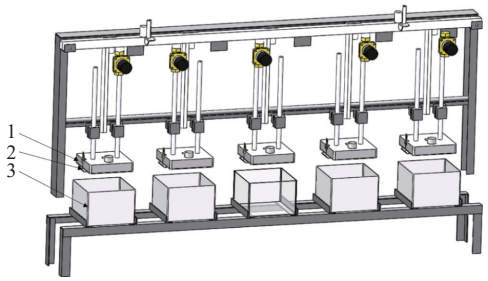

Note: 1. Suction box 2. Restrictor 3. Materials box

Figure 12 Schematic diagram of the feeding mechanism

As the key functional component of the feeding mechanism, the adsorption of cassia seeds significantly impacts the efficiency of the feeding process. The suction box consists of two main parts: the suction plate and the box itself. The suction plate features uniformly distributed holes, and its structural parameters, as well as the material level design of the lower grinding disk, are consistent. The primary focus in this context is on the hole size and the vacuum design.

1) Suction disk

According to the agricultural machinery design manual[22], the diameter of the suction holes in the seed-discharging disk of air-assisted seeders should be determined based on the size of the seeds being processed.

$$D = (0.6 \sim 0.8)\bar{S} \tag{10}$$

where, D is the diameter of the suction hole, mm; $\bar{S}$ is the average value of the three axis dimensions of the seeds, mm.

Initial pre-experimental investigations revealed a substantial variation in the triaxial dimensions of cassia seeds, which resulted in a tendency for the seeds to be adsorbed along their long axis. It was observed that when the pore diameter of the suction plate exceeded a certain threshold, the volume of adsorbed material increased significantly. However, an excessively large pore diameter led to frequent occurrences of seeds becoming lodged in the holes during the unloading process. Conversely, when the pore diameter was too small, the seeds also tended to become stuck, but to a greater extent, due to increased friction and resistance. A force analysis of this phenomenon is presented in Figure 13.

The forces on cassia in the adsorbed state are satisfied:

$$G \leq f + T \tag{11}$$

where, f is the friction force of the sidewalls of the aperture on the cassia seeds, N; T is the suction force generated by the vacuum chamber on the seeds, N.

With larger orifices, a greater portion of the seed volume enters each hole, increasing the contact area with the sidewalls and thereby

generating greater friction. During the unloading phase, as the vacuum created by the negative pressure system dissipates and the suction force approaches zero, the residual frictional force may still counteract the gravitational force, causing seeds to remain lodged within the orifices. These retained seeds block the affected orifices, preventing them from supplying raw material in subsequent grinding cycles and thus reducing the overall grinding efficiency. To mitigate this issue, a coefficient of 0.6 was applied in the orifice diameter calculation, resulting in a final orifice size of 0.8 mm.

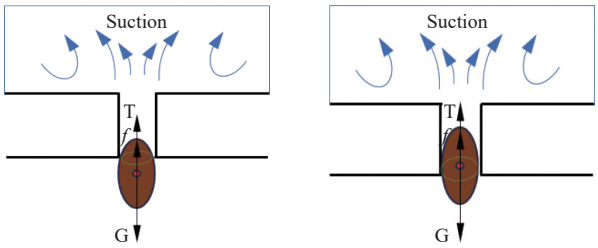

a. Small diameter b. Large diameter

Figure 13 Schematic diagram of the force of cassia in the hole

2) Vacuum level inside the box

Referring to the agricultural machinery design manual[22], the design of suction holes in the seed discharge tray of air-absorbent seed sowing machines stipulates that the vacuum pressure within the suction box must exceed the minimum vacuum required to adsorb a single seed. Taking into account the structural configuration of the feeding mechanism and the specific motion characteristics involved, the required vacuum level within the suction box is calculated as follows:

$$H_{cmax}=\frac{80K_1K_2mgh}{\pi d_1^3}\left(1+\frac{2v_s^2}{gD}+\lambda\right) \tag{12}$$

where, m is the mass of a single seed, g; h is the distance between the center of the seed and the suction disk, mm; v_s the moving speed of the suction disk, mm/s; D is the diameter of the imitation hole of the suction disk, mm; g is the acceleration of gravity; λ is the integrated coefficient of the frictional resistance of the seed; K_1 is the reliability coefficient of the suction of the seed with the values from 1.8 to 2.0; K_2 is the coefficient of the external conditions, with the values ranging from 1.6 to 2.0.

Based on the material properties of cassia seeds, the given parameters are as follows[22]: g=9.8 m/s^2, λ=6, K_1=1.9, and K_2=1.8. After applying these values to Equation (9), the calculated result is –4 to –5 kPa.

2.3.3 Negative pressure system

To ensure the stable operation of the feeding mechanism, it is critical to accurately calculate and select an appropriate negative pressure system. The negative pressure within the loading mechanism must be maintained within the range of –4 to –5 kPa. Additionally, the relationship between inlet and outlet flow rates must be considered to maintain system balance. Given the relatively small differential pressure designed in this study, the subsonic flow calculation equation is most suitable for accurately determining the system's airflow characteristics.

$$Q_C=C_dA\sqrt{\frac{2\Delta P}{\rho}} \tag{13}$$

where, Q_C is the volumetric flow rate, m^3/s; C_d is the flow coefficient, related to the shape and size of the pipeline, with a value in the range of 0.6 to 0.9; A is the cross-sectional area of the pipeline, m^2; ΔP is measured in pascals, Pa; ρ is the density of the gas, kg/m^3.

In this study, the cross-sectional area of the pipe is defined as the sum of the cross-sectional areas on the suction disk. To ensure that the negative pressure is stabilized, the calculation is made in accordance with the maximum pipe area, which represents the simultaneous operation of all loading mechanisms.

$$A=z\pi\left(\frac{D}{2}\right)^2 \tag{14}$$

The cross-sectional area of the pipe is calculated to be 1.005×10^{-3} m^2. The pipe is a standard round hole, and the flow coefficient is taken to be 0.7. The pressure difference is set to the maximum value of vacuum, −5 kPa. Finally, ρ represents the density of air, which is 1.225 kg/m^3. Subsequently, the Equation (10) was employed to ascertain that Q_c equates to 63.7 m^3/h.

In consideration of the calculations, as well as the potential for air leakage or volume leakage calculation errors during the connection process, a rotary vane vacuum pump with a higher working flow rate per unit time (XD-100) was selected as the negative pressure air source, with a working flow rate of Q_t= 100 m^3/h. In accordance with the operational specifications of the vacuum pump, a single run must exceed a minimum duration of three hours. If the vacuum pump is employed as a negative pressure system without an intervening buffer, the phenomenon of continuous starting and stopping will occur, thereby reducing the service life of the pump. To address this phenomenon, a buffer tank is installed between the vacuum pump and the machine. To guarantee the stable operation of the vacuum pump, the single-cycle working time was established at three hours. Furthermore, the vacuum pump was activated five minutes prior to the commencement of the grinder. To ascertain the volume of the buffer tank, the program was utilized.

$$V_c=Q_t\cdot t_1+(Q_t-Q_C)t_2 \tag{15}$$

After calculating the volume of the buffer tank, it was determined that a volume of 150 L would be optimal, given the circumstances. Moreover, the tank is equipped with a digital electric contact pressure gauge, which serves to guarantee that the negative pressure within the tank remains within a specified range of stability. Following numerous trials, the negative pressure threshold has been determined to be between −4 and −5 kPa. The vacuum pump is initiated when the upper limit is reached and terminated when the lower limit is reached. The vacuum pump, buffer tank, and pressure gauge collectively constitute the negative pressure closed-loop system's three primary components, as illustrated in Figure 14.

Note: 1. Buffer tank 2. Pressure gauge 3. Vacuum pump

Figure 14 Schematic diagram of negative pressure system

2.3.4 Transport mechanism

The transport mechanism is composed of a stepping motor, a synchronous gear group, a worm gear, and a translation tray. According to the actual process requirements, the total length of the screw is set to 1500 mm, and the common pitch of the screw is 5/10/20/40 mm. The larger the pitch, the larger the lead. However, considering the economy and cost, the 10 mm pitch is chosen, that is, the screw turns one circle and the plate is moved 10 mm. In addition, the ratio of the diameter of the synchronous gear on the motor shaft to the diameter of the synchronous gear on the screw is 2:1. By using a synchronous belt drive, the motor rotates one circle while the screw rotates two circles, which indirectly increases the translation speed[23–24].

2.4 Control system design

The electrical control system consists of a single-chip microcomputer and its peripheral circuitry, a stepping motor, a DC motor, a relay module, and travel switches, among others. It has a built-in 5/24/48/110 V DC power supply, and the block diagram of the control system is shown in Figure 15.

The stepping system is used for grinding, translating, lifting/falling of the lower grinding disk, and rising/falling of the scraper. This allows the speed and stroke to be adjusted according to different processing requirements.

Among them, the speed of the translational motor affects the overall production efficiency. The characteristics of the stepping motor are that torque decreases as the speed increases, and the rated load is typically 0-1000 r/min, and the torque essentially basically zero at 1000 r/min[25–26]. According to the Equation (16):

$$n_c = f_c \times \frac{60b}{200} \tag{16}$$

where, n_c is the motor speed, r/min; f is the pulse frequency, Hz; b is the subdivision multiple. The motor driver is set to the secondary subdivision mode (400 pulses equals one revolution). In the case of different speeds, Table 5 illustrates the relationship between time, speed, and pulse frequency required to traverse a distance of 1300 mm.

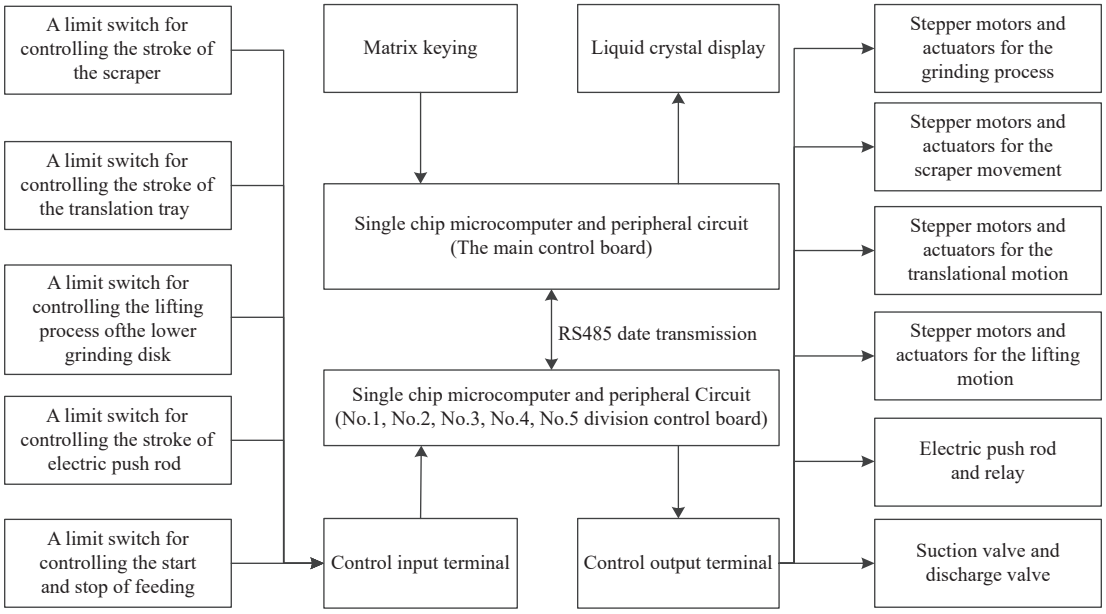

Figure 15 Diagram of control system composition block

Table 5 Relation between speed and parameters

Motor speed/ r·min^{-1}	Translation time/ s	Translation velocity/ m·s^{-1}	Pulse frequency/ Hz
1000	7.80	0.17	6666
800	9.75	0.13	5333
600	13.00	0.10	4000
400	19.50	0.07	2666
200	39.00	0.03	1333

The DC motor is relatively simple to use compared with the stepper motor. In this system, it is used in conjunction with the relay to achieve the purpose of forward/reverse rotation of the suction electric push rod[27–29].

In the same way, RS485 communication between the main control board and the five control boards can be realized through the human-computer interaction panel. Users can query the grinding pressure level, grinding time, and other information parameters of each pipeline in real time, and change these parameters according to the actual machining accuracy requirements. The flow chart is shown in Figure 16.

Whether it is the main control board or the section control board, the software programming uses the Keil 5 platform and the functional

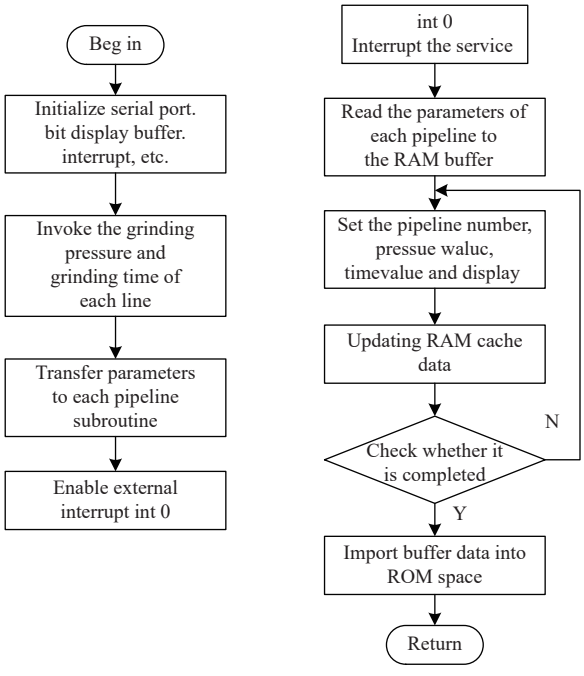

Figure 16 Flowchart for communication services

modular design approach. This includes subprograms such as system initialization, communication, actuator operation (grinding, lifting, loading/unloading, etc.), key processing, and digital display.

The subroutine corresponds to the corresponding circuit, which facilitates the coordination and integration between the hardware and software of the system.

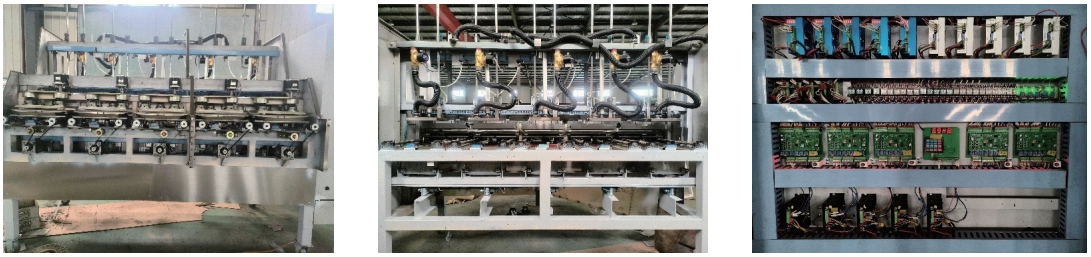

a. Workstation A b. Workstation B c. Control cabinet

Figure 17 Structure schematic diagram of the cassia grinding machine

2.5 Performance tests

To test the performance of the designed cassia grinding machine, a prototype was built and tested as shown in Figure 17. The analysis and calculation conducted during the design process revealed that the gap of the grinding layer, the grinding time, and the grinding speed exert a considerable influence on the operational performance of the submerged device. To assess the impact of these three factors on the grinding device's performance, a performance test was conducted[30–32].

2.6 Test methods

The test was calculated in accordance with the methodology delineated in GB/T 21719-2008. Prior to the commencement of the experiment, a sample of cassia seeds of the same grade was selected as the test object. The experiment was conducted in accordance with the operational steps of the machine safety protocol. Photographic documentation was undertaken of the cassia seeds both before and after the test. The test was repeated three times, with photographic documentation undertaken on each occasion under the same parameter conditions. The mean value was obtained from the three sets of images and represents the final test result[33–36].

2.7 Test indicators

The grinding degree and crushing rate were selected as the test indices, with the calculation presented in the following equation:

$$\mathrm{DOM}=\left(1-\frac{M_1}{M_0}\right)\times 100\% \tag{17}$$

$$Y_c=\frac{M_B}{M_K}\times 100\% \tag{18}$$

where, DOM represents the grinding degree of the grain, %; M_1 represents the quality of the sample after grinding, g; M_0 represents the quality of the sample before grinding, g; Y_c represents the crushing rate of the grain, the unit is %; M_B represents the mass of the broken grain, g; M_K represents the mass of the sample after grinding, g.

According to GB/T 21719-2008, the process involves brushing off any remaining powder and selecting grains that are less than half the length of complete grains as broken grains. These broken grains are then weighed.

Above indicators are evaluated through a comprehensive grinding assessment, encompassing both the overall quality and the specific effects of grinding. This approach allows for a holistic evaluation of the grinding effect, which is not feasible when examining the impact of a single grain. To more effectively respond to the grinding effect of a single grain, this study employs image recognition to extract the light reflectivity of the cassia seed surface after grinding under different test factors. This is then linked with the grinding degree to establish a standard for evaluating the grinding effect of a single grain of cassia seed.

$$\eta=\frac{P_1}{P_2} \tag{19}$$

where, η is the light reflectivity of the cassia seed surface; P_1 is the area of white refracted light on the surface, candela/m^2; and P_2 is the effective area of refracted light on the surface, candela/m^2.

2.8 Single-factor test

2.8.1 The influence of grinding layers spacing on grinding effect

In the test of the influence of the gap between the grinding layers on the grinding effect, the factor B was set at 120 r/min, and the factor C was 12 s. According to the measurement results of cassia seed size, the spacing of the upper and lower grinding disks was adjusted sequentially to 1.2 mm, 1.8 mm, 2.4 mm, 3.0 mm, and 3.6 mm.

2.8.2 The influence of grinding speed on grinding effect

In the test to determine the impact of the rotation speed of the grinding motor on the grinding effect, factor A was set at 2.4 mm and factor C at 12 s. The rotation speed was adjusted to 60 r/min, 120 r/min, 180 r/min, 240 r/min, and 300 r/min.

2.8.3 The influence of grinding time on grinding effect

In the test to determine the impact of grinding time on the grinding effect, factor A was set at 2.4 mm, while factor B was set at 120 r/min. The time intervals were adjusted to 10 s, 12 s, 14 s, 16 s, and 18 s.

3 Results and discussion

3.1 Single-factor test

As illustrated in Figure 18a, when the grinding layer gap is set to 1.2 mm, the resulting pressure is excessive, leading to a high crushing rate and a low grinding degree. As the gap increases, the grinding degree first improves and then declines, while the crushing rate decreases. This indicates that increased spacing reduces the frictional and compressive forces exerted on the cassia seeds, thereby lowering the grinding effectiveness. Therefore, it is recommended to maintain the grinding layer gap within the range of 1.8-3.0 mm to achieve an optimal balance between grinding efficiency and seed integrity.

As illustrated in Figure 18b, with an increase in motor speed, the grinding degree shows noticeable fluctuations. When the speed exceeds 180 r/min, cassia seeds tend to collide and compress against each other more frequently, resulting in a significantly higher crushing rate. To ensure stable grinding performance while minimizing damage to the seeds, it is advisable to control the motor speed within the range of 60-180 r/min.

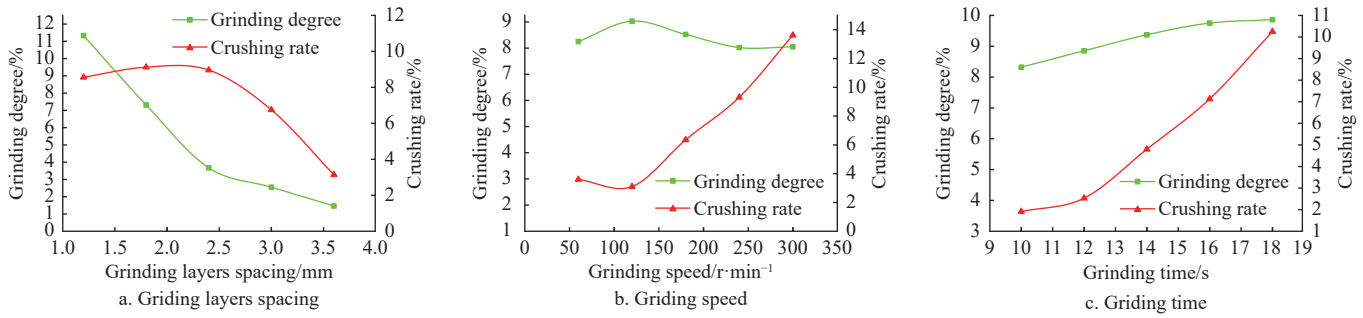

Figure 18 Results analysis of single factor test

As illustrated in Figure 18c, when the grinding time is less than 12 seconds, the grinding process is insufficient, leading to both a low grinding degree and low crushing rate. At around 12 seconds, the grinding degree reaches a relatively high value. However, extending the grinding time beyond 14 seconds causes excessive grinding, which increases the crushing rate. Therefore, the recommended grinding time is within the range of 10-14 seconds to ensure efficient and uniform surface treatment of cassia seeds.

3.2 Optimization test

The test scheme and results are listed in Table 6.

Table 6 Results of orthogonal experiments

No.	A/mm	B/r·min^{-1}	C/s	Grinding degree/%	Crushing rate/%
1	2.4	60	14	8.87	4.04
2	1.8	180	12	8.94	7.55
3	1.8	120	14	8.94	7.43
4	2.4	120	12	9.14	3.69
5	1.8	120	10	9.01	7.10
6	3.0	180	12	7.12	3.11
7	2.4	180	14	9.13	5.10
8	2.4	120	12	9.21	3.67
9	2.4	180	10	8.99	5.02
10	3.0	60	12	7.05	2.98
11	3.0	120	10	7.07	3.06
12	2.4	120	12	9.13	4.06
13	1.8	60	12	9.03	7.20
14	2.4	60	10	8.77	3.94
15	3.0	120	14	7.08	3.17
16	2.4	120	12	9.03	3.96
17	2.4	120	12	9.12	4.06

3.2.1 Grinding degree

The results of the experiment were imported into the Design Expert 13 for analysis of variance, and the e ANOVA analysis of grinding degree results are organized into Table 7 for subsequent analysis.

The model p<0.0001 (<0.01) shows that the regression model of the grinding degree is extremely significant, and the regression equation is meaningful. The model misfit term p=0.1324 (>0.05) is not significant, indicating that the fitting level of the equation is high and significant.

The effects of the interaction of various experimental factors on the grinding degree of cassia seeds are illustrated in Figure 19. The interaction of A-B, A-C, and B-C has a significant impact on the degree of grinding. The interaction surface undergoes notable alterations in response to alterations in the spacing of the grinding gap, the grinding speed, and the grinding time. The interaction surface exhibits the most gentle changes between the grinding speed and grinding time. As illustrated in Figure 19a, the grinding degree exhibits a biphasic response to changes in the spacing and rotation speed, initially increasing and then decreasing at the same grinding time. As illustrated in Figure 19b, at a constant speed, the degree of grinding initially increases and then decreases with an increase in both spacing and grinding time. Figure 19c illustrates that when the grinding gap spacing is maintained at a constant level, the degree of grinding exhibits slight fluctuations in response to variations in grinding speed and time.

Table 7 ANOVA analysis of grinding degree

Source	Grinding degree variance analysis				
	Sum of Squares	*df*	Mean Square	*F*-value	*p*-value
Model	11.680	9	1.300	153.99	<0.0001
A	7.220	1	7.220	856.32	<0.0001
B	0.027	1	0.027	3.14	0.1198
C	0.004	1	0.004	0.48	0.5106
AB	0.006	1	0.006	0.76	0.4125
AC	0.002	1	0.002	0.19	0.6762
BC	0.001	1	0.001	0.05	0.8338
A2	4.240	1	4.240	502.39	<0.0001
B2	0.033	1	0.033	3.87	0.0900
C2	0.041	1	0.041	4.80	0.0647
Residual	0.059	7	0.008	-	-
Lack of Fit	0.043	3	0.014	3.43	0.1324
Pure Error	0.017	4	0.004	-	-
Cor Total	11.740	16	-	-	-

3.2.2 Crushing rate

An ANOVA of the crushing rate was conducted, and the results are shown in Table 8.

Table 8 ANOVA analysis of crushing rate

Source	Crushing rate variance analysis				
	Sum of Squares	*df*	Mean Square	*F*-value	*p*-value
Model	42.27	9	4.70	63.20	<0.0001
A	35.96	1	35.96	483.84	<0.0001
B	0.86	1	0.86	11.55	0.0115
C	0.05	1	0.05	0.65	0.4478
AB	0.01	1	0.01	0.16	0.6986
AC	0.01	1	0.01	0.16	0.6986
BC	0.01	1	0.01	0.01	0.9718
A2	4.16	1	4.16	55.93	0.0001
B2	0.46	1	0.46	6.11	0.0427
C2	0.41	1	0.41	5.39	0.0532
Residual	0.52	7	0.07	-	-
Lack of Fit	0.37	3	0.12	3.26	0.1419
Pure Error	0.15	4	0.04	-	-
Cor Total	42.79	16	-	-	-

The model $p<0.0001$ (<0.01) shows that the regression model of the grinding degree is extremely significant, and the regression equation is meaningful. The model misfit term $p=0.1419$ (>0.05) is not significant, indicating that the fitting level of the equation is high and significant.

The effects of the interaction of various experimental factors on the crushing rate of cassia seed are illustrated in Figure 20. The interaction of A-B, A-C, and B-C has a significant impact on the crushing rate. The interaction between the grinding gap spacing and the grinding speed, as well as the grinding gap spacing and the grinding time, has a considerable impact on the interaction surface. Figure 20a illustrates that, under identical grinding times, the crushing rate declines with increasing spacing and rises with elevated rotational speeds. As illustrated in Figure 20b, at a constant speed, the crushing rate decreases with an increase in spacing and exhibits a slight increase with an increase in grinding time. Figure 20c illustrates that when grinding gap spacing is maintained at a constant level, the crushing rate exhibits a slight increase with an increase in grinding speed and time.

The objective was to identify the optimal parameters for maximizing the grinding degree and minimizing the crushing rate. The objectives are as follows: The objectives of the three factors were set within the range of optimization. The results demonstrated that the optimal combination of working parameters was attained when the grinding disk spacing was 2.342 mm, the grinding speed was 169.801 r/min, and the grinding time was 12.273 s. The grinding degree was 9.19%, and the crushing rate was 4.62%. This combination of parameters exhibited the most favorable outcomes.

In accordance with the optimization outcomes of the trial, the parameters were rounded to a grinding gap spacing of 2.4 mm, a grinding speed of 170 r/min, and a grinding time of 12 s, after which a verification test was conducted. The measured grinding degree was 9.07%, while the crushing rate was 4.51%. The discrepancy between the verification outcomes and the model optimization results is minimal, suggesting that the optimization outcomes are highly reliable.

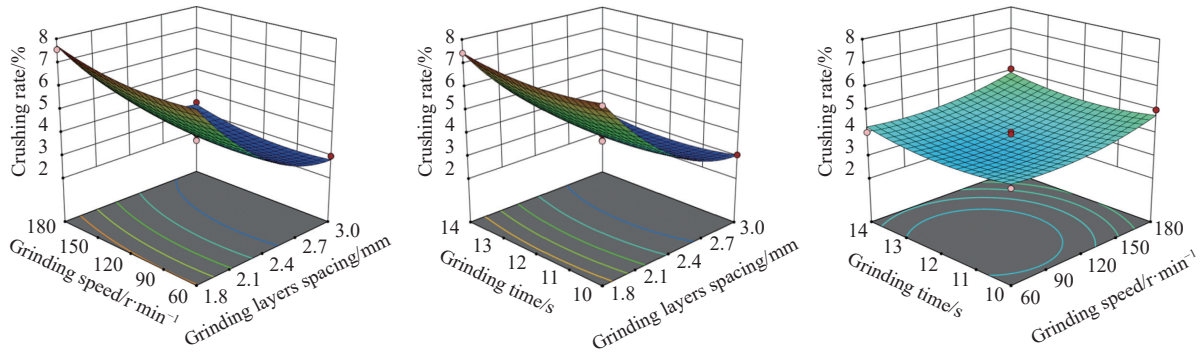

a.Interaction of factors A and B b. Interaction of factors A and C c. Interaction of factors B and C

Figure 19 Response surface chart of grinding degree

3.3 Crushing rate and light reflectivity

The test results show that when the grinding time is less than 12 seconds, the grinding is not sufficient, resulting in a low grinding degree and crushing rate. When it reaches 12 seconds, the grinding degree reaches a higher value. When the grinding time exceeds 14 seconds, it leads to a longer duration, which in turn increases the rate of grain crushing. Therefore, it is more appropriate to control the grinding time between 10 and 14 seconds.

To digitize the grinding degree of single seeds[37–40], the surface features were extracted using a variety of grinding degree of cassia seeds, and the resulting effect is illustrated in Figure 21. As can be observed through comparison, the surface light reflectivity of cassia seeds diminishes in conjunction with the escalation of the crushing rate. To confirm the linear correlation between crushing rate and light reflectance, 100 randomly selected seeds with different grinding degree were plotted for surface characterization. The resulting scatter plots of grinding degree versus surface opalescence rate are presented in Figure 22.

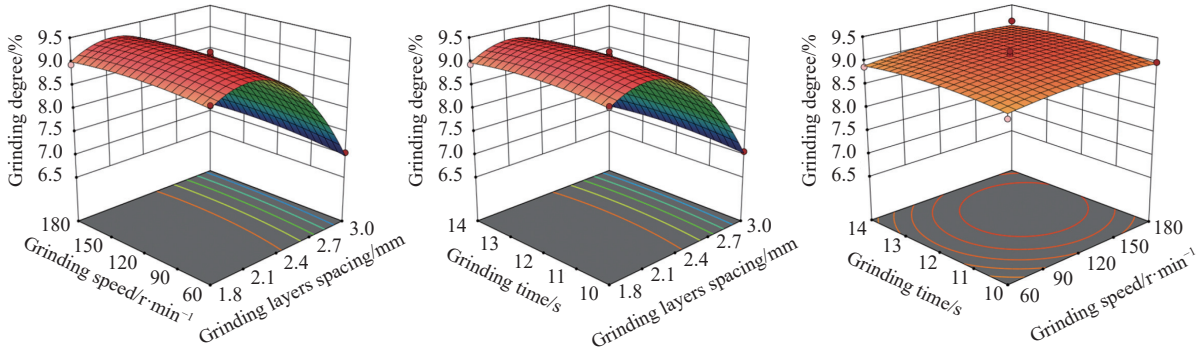

a.Interaction of factors A and B b. Interaction of factors A and C c. Interaction of factors B and C

Figure 20 Response surface chart of grinding degree

It can be observed that the thin shell on the surface of cassia seeds can be removed by grinding, as demonstrated by the grinder. The grinding degree of cassia seeds exhibits a negative linear relationship with the refractive index of light, with a high degree of linearity (R^2=0.943 94). Additionally, the surface roughness of cassia seeds increases with the grinding effect, which subsequently reduces the refractive index of white light. The linear fitting equation of cleaning rate to refractive index was obtained using

Origin software.

$$y = 9.475 - 0.338\ 25x \tag{20}$$

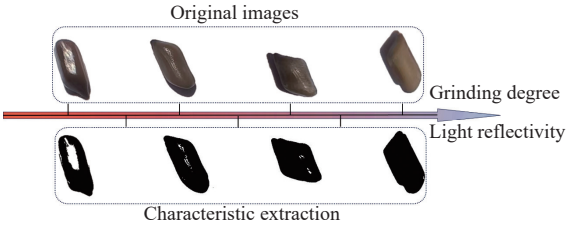

Figure 21 Schematic diagram of the original image versus the characteristic extraction

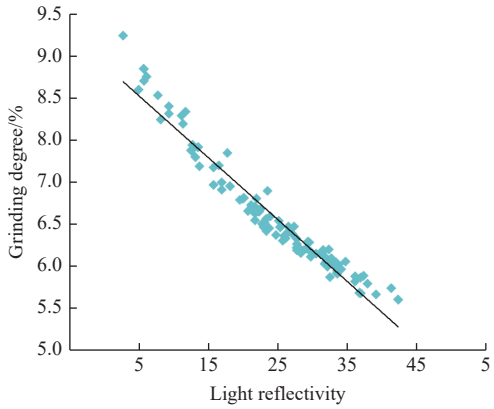

Figure 22 Schematic diagram of the original image versus the characteristic extraction

4 Conclusions

The following conclusions were drawn from the study:

1) A kneading cassia grinding machine was designed to replicate the hand-kneading action, specifically adapted to the properties of cassia seeds.

2) Key parameters of the grinding device were determined through analysis and evaluation of cassia seed grinding dynamics. The upper grinding disk has a diameter of 6 mm, while the lower grinding disk has a diameter of 13 mm. The suction disk contains 100 uniformly spaced holes, each with a diameter of 0.8 mm and 6 mm apart. The vacuum within the cassette ranges from –2 to –5 kPa.

3) The equipment employs a modular design with a clear structural division of hardware and software systems. Required functions are achieved through scientific methods, including experimental techniques. The prototype enables full automation of the cassia seed grinding and processing process, providing excellent stability and scalability. The control system enables RS485 communication between control panels, allowing users to modify operating parameters in real time via human-computer interaction.

4) The grinder's performance was evaluated through one-way and orthogonal tests to identify the optimal parameter combination. The best parameters produced a grinding degree of 9.07% and a cleanliness rate of 4.51% when the grinding layer gap was 2.4 mm, with a grinding speed of 170 r/min and a grinding time of 12 s. The minimal discrepancy between the test results and the analyzed outcomes falls within an acceptable range.

5) A linear relationship between grinding degree and characteristic extraction was demonstrated by measuring the surface photorefractive index of milled cassia seeds, with the grinding degree digitized as a discrete value for each grain.

[References]

[1] Lam W C, Lyu A P, Bian Z X. ICD-11: impact on traditional Chinese medicine and world healthcare systems. Pharmaceutical medicine, 2019; 33: 373–377.

[2] Zhou X, Li C G, Chang D, Bensoussan A. Current status and major challenges to the safety and efficacy presented by Chinese herbal medicine. Medicines, 2019; 6(1): 14.

[3] Wu D T, Liu W, Han Q H, Wang P, Xiang X R, Ding Y, et al. Extraction optimization, structural characterization, and antioxidant activities of polysaccharides from cassia seed (*Cassia obtusifolia*). Molecules, 2019; 24(15): 2817.

[4] Pachpor A, Kulkarni D V, Dongre P, Bhaldar N, Khandekar S, Maurya S. A clinical study on effect of Cassia tora Linn: In drug resistance case of tinea corporis. Word Journal of Pharmacy and Pharmaceutical Sciences, 2019; 8(9): 730–738.

[5] Wu X, Wang S P, Lu J R, Jing Y, Li M X, Cao J L, et al. Seeing the unseen of Chinese herbal medicine processing (Paozhi): advances in new perspectives. Chinese Medicine, 2018; 13: 4.

[6] Qamar S Z, Pervez T, Chekotu J C. Die defects and die corrections in metal extrusion. Metals, 2018; 8(6): 380.

[7] Jayasimha S L N, Bawge G, Raju H P. Surface finish characteristics of distinct materials using extrusion honing process. Journal of Computational & Applied Research in Mechanical Engineering (JCARME), 2021; 12(1): 41–50.

[8] Hou J M, Liu X, Zhu H J, Ma Z, Tang Z Y, Yu Y C, et al. Design and motion process of air-sieve castor cleaning device based on discrete element method. Agriculture, 2023; 13(6): 1130.

[9] Balcı F, Bayram M. Modification of mechanical polishing operation using preheating systems to improve the bulgur color. Journal of Cereal Science, 2017; 75(5): 108–115.

[10] Kang D, Wang Y, Fan Y H, Chen Z J. Research and development of Camellia oleifera fruit sheller and sorting machine. IOP Conference Series: Earth and Environmental Science, 2018; 108(4): 042051.

[11] Wang G L, Wang Y Q. Research on polishing process of a special polishing machine tool. Machining Science and Technology, 2009; 13(1): 106–121

[12] Qu X T, Zhang H, Zhao Y B, Zhang F Q. Dynamic design of grinding and polishing machine tool for blisk finishing. IOP Conference Series Materials Science and Engineering, 2018; 382(4): 042014.

[13] Caringal B K M, Rosa Z S D, Maan K V R, Camello N C. Design and development of rice milling and grinding machine. International Journal of Science and Engineering, 2016; 2(3): 5–12.

[14] Kalagbor I, Fyneface D, Korfii U, Ogaji T, Kpoonanyie F. Estimation of the levels of Fe in wheat and maize flour milled using commercial milling machine and a home blender. Journal of Applied Sciences and Environmental Management, 2017; 21(2): 341–344.

[15] Ratnavathi C V. Sorghum processing and utilization. In: Ratnavathi C V, Patil J V, Chavan U D, editors. Sorghum Biochemistry. Academic Press, 2016; pp.311–327. doi: 10.1016/B978-0-12-803157-5.00006-X

[16] Zamri R, Ismail N, Hang Tuah bin Baharudin B T, Mohamed Ariff A H, Prabuwono A S. Analysis of flat and dry polishing parameter influence on surface roughness for robotic polishing cell. Applied Mechanics and Materials, 2014; 564: 543–548.

[17] Dieste J A, Fernández A, Roba D, Gonzalvo B, Lucas P. Automatic grinding and polishing using spherical robot. Procedia Engineering, 2013; 63(9): 938–946.

[18] Melentiev R, Fang F. Recent advances and challenges of abrasive jet machining. CIRP Journal of Manufacturing Science and Technology, 2018; 22(8): 1–20.

[19] Alsoufi M S. State-of-the-art in abrasive water jet cutting technology and the promise for micro-and nano-machining. International Journal of Mechanical Engineering and Applications, 2017; 5(1): 1–14.

[20] Guo C S, Shi Z D, Mullany B, Linke B, Yamaguchi H, Chaudhari R, et al. Recent advancements in machining with abrasives. Journal of Manufacturing Science and Engineering, 2020; 142(11): 110810.

[21] Krutz G, Thompson L, Claar P. Design of agricultural machinery. John Wiley and Sons: 1984. 480p.

[22] Sciences C. A. o. A. M. Agricultural Machinery Design Manual. 2007.

[23] Hu Y J, Wang Y, Zhu W, Li H. Dynamic modeling of a ball-screw drive and identification of its installation parameters. Journal of Dynamic Systems, Measurement, and Control, 2021; 143(4): 041003.

[24] Lai C K. The Research of stepper motor subdivision control system for

cloth-cutting machines. Applied Mechanics and Materials, 2014; 443(10): 285–289.

[25] Xu Y F, Zhang X L, Wu S, Chen C, Wang J Z, Yuan S Q, et al. Numerical simulation of particle motion at cucumber straw grinding process based on EDEM. Int J Agric & Biol Eng, 2020; 13(6): 227–235.

[26] Stockl A, Loeffler D, Oechsner H, Jungbluth T, Fischer K, Kranert M. Near-infrared-reflection spectroscopy as measuring method to determine the state of the process for automatic control of anaerobic digestion. Int J Agric & Biol Eng, 2013; 6(2): 63–72.

[27] Hou J M, Yao E C, Li J P, Bai J B, Yang Y, Zhu H J. Motion analysis and experiment on shelling process of kneading and pressing castor shelling machine. Transactions of the Chinese Society for Agricultural Machinery, 2018; 51(s2): 220–232. (in Chinese)

[28] Shi M C, Liu M Z, Li C H, Cao C M, Li X P. Design and experiment of cam rocker bidirectional extrusion walnut shell breaking device. Transactions of the CSAM, 2022; 53(1): 140–150. (in Chinese)

[29] Wan Z H, Zhang G Z, Xu H M, Zhou Y, Tang N R, Zhang H. Design and experiment of the clamping sheller for fresh water caltrop. Transactions of the CSAE, 2022; 38(20): 9–19. (in Chinese)

[30] Zhu G F, Ren J J, Wang Z, Xiang H, Mu R S, Li S H. Design of shelling machine for camellia oleifera fruit and operating parameter optimization. Transactions of the CSAE, 2016; 32(7): 19–27. (in Chinese)

[31] Tang J Y, Wang D, Kou X, Qu Z X, Xu K S. Design and experiment of four-channel fully automatic shelling machine for ripe fresh camellia oleifera fruit. Transactions of the CSAM, 2021; 52(4): 109–116,229. (in Chinese)

[32] Wang J N, Liu M J, Cao M Z, Yan J C, Peng B L, Hu Z C, et al. Working parameter optimization and experiment of key components of coix lacryma-jobi sheller. Transactions of the CSAE, 2018; 34(13): 288–295. (in Chinese)

[33] Zhan G C, Ma L N, Huang X M, Zong W Y, Tian W, Lin Z X. Experimental study on impact crushing of rapeseed stalks during threshing of oilseed rape. Transactions of the CSAE, 2020; 36(24): 11–18. (in Chinese)

[34] Li J, Lu H Z, Yang Z L, Chen Z L, Huang J C. Design and experiment of Canavalia shelling mechanism. Transactions of the CSAE, 2013; 29(1): 26–32. (in Chinese)

[35] Zhang Q, Ding W, Deng L, Li Y, Zhao Y. Experimental study on friction characteristics of gorgon nuts (Euryale ferox) in mechanical shelling. Transactions of the CSAE, 2013; 29(1): 56–63. (in Chinese)

[36] Xu X Q, Rao H H, Li T, Liu M H. Design and experiment on automatic husking and peeling machine for lotus seeds. Transactions of the CSAE, 2014; 30(13): 28–34. (in Chinese)

[37] Zhang L H, Xu Z M, Gou W, Ma Z Y. Optimization of structure parameters of cylinder-bar type shelling device for ginkgo biloba. Transactions of the CSAE, 2012; 28(10): 39–45. (in Chinese)

[38] Araque O, Arzola N, Cerón I X. Microstructure and mechanical characterization of rice husks from the tolima region of Colombia. Resources, 2024; 13(1): 16.

[39] Liao P, Meng Y, Chen Y Q, Weng W N, Chen L, Xing Z P, et al. Potted-seedling machine transplantation simultaneously promotes rice yield, grain quality, and lodging resistance in China: A meta-analysis. Agronomy, 2022; 12(12): 3003.

[40] Liu X P, Shi Z A, Zhang Y L, Li H, Pei H C, Yang H J. Characteristics of damage to brown rice kernels under single and continuous mechanical compression conditions. Foods, 2024; 13(7): 1069.